

# Robust Localization and Classification of Barely Visible Indentations in Composite Structures by Fusion of Ultrasonic Damage Indices

**Mohammad Ali Fakih**

Laboratory of Smart Structures and Structural Integrity (SSSI),  
Department of Mechanical Engineering,  
American University of Beirut,  
Beirut 1107 2020, Lebanon  
e-mail: mh17@mail.aub.edu

**Samir Mustapha<sup>1</sup>**

Laboratory of Smart Structures and Structural Integrity (SSSI),  
Department of Mechanical Engineering,  
American University of Beirut,  
Beirut 1107 2020, Lebanon  
e-mail: sm154@aub.edu.lb

**Ali Abdul-Aziz**

Department of Aerospace Engineering,  
Kent State University,  
Kent, OH 44242  
e-mail: aabdula3@kent.edu

*This study aims to detect, localize, and assess the severity of barely visible indentation damage in a composite sandwich structure using ultrasonic guided waves. A quasistatic loading was gradually applied on a specimen of carbon fiber reinforced epoxy resulting in dents on the surface. Lamb-wave measurements, from a sensor network mounted on the panel's surface, were taken for the intact condition and three damage cases (0.2, 0.5, and 2.7-mm dents). Three approaches were adopted to define the damage indices (DIs) toward anomaly detection, namely, amplitude variation, symbolic dynamics, and root mean square deviation. Data fusion was performed between measurements from multiple excitation frequencies for single and multiple DIs, where the anomaly combination between all the frequencies and the DIs was called a total anomaly. An imaging algorithm was implemented for damage localization in conjunction with single and combined DIs. It was shown that combining the effects of different frequencies and/or different DIs increases the robustness and consistency of the damage detection and localization process. Moreover, a distance-based classification technique was applied using features from single DIs and the combined anomaly measure. Accuracies higher than 91% were attained for the majority of the cases tested. [DOI: 10.1115/1.4044177]*

*Keywords: barely visible indentation damage, composite sandwich structures, guided waves, fusion of damage indices, damage detection, damage localization, damage classification, ultrasonics*

## 1 Introduction

The high specific strength and high bending stiffness of composite sandwich structures have made them good candidates for application in various fields, such as aerospace, marine, and civil structures. Composite structures are prone to various forms of damage, including fiber breakage, matrix cracking, and delamination [1,2]. Low-velocity impacts caused by various sources such as bird strikes (while an aircraft is parked or during taxiing) [3], tools dropped on parts during manufacture and servicing, or runway debris encountered during takeoff can easily crush the core and result in a dent on the surface of the panels [4,5]. Such impact loading usually produces hidden damage, known as barely visible indentation damage (BVID). BVID can result in a noticeable decrease in the load-carrying capability of the material [6], and such damage can develop progressively, leading to a catastrophic failure [7].

The involvement of such structures in critical applications entails the need for evaluation methods to assess their integrity while being in service. Damage detection in composite sandwich structures is particularly difficult because the skin-core configuration conceals damage. Various nondestructive testing (NDT) based methods, such as the instrumented tap tester and air-coupled transmission ultrasonic C-scanning, are currently in use for inspection and evaluation of sandwich structures. Ruzek et al. [8] compared different detection methods including visual, C-scan, and shearography to inspect a composite sandwich structure after impact. C-Scan was not very suitable for BVID detection, but shearography performed

better and, as expected, the visual method was not efficient. Further, the capability of fiber Bragg grating sensors to detect BVID in composite wing structures was demonstrated during integrity tests after the impact [9]. Takeda et al. [9] identified the damage by monitoring the change in the signals of the fiber Bragg grating sensors due to the presence of damage.

The applicability of guided waves for detection and characterization of flaws and defects was the focus of many researchers for the last three decades. In particular, Lamb waves have the ability to travel for long distances in complex structures, and hence they can be a good candidate for application in the field of structural health monitoring (SHM). Lamb waves have been used to detect various types of damage in composites and metallic structures, including corrosion, fatigue cracking, delamination, fiber breakage, and debonding [10–17].

Much research has focused on capturing BVID in composite and metallic structures based on elastic waves. Polimeno and Meo [18] implemented a nonlinear elastic wave spectroscopy to detect BVID in carbon fiber reinforced epoxy (CF/EP) composites, based on the shift in resonance frequency or the presence of harmonics and sidebands contained within the signals. Ross [19] and Zhang et al. [20] proposed piezoelectric sensor networks for real-time monitoring of structures to detect the location and time history of impact forces; the authors aimed at detecting impacts at the time they occurred and to locate them according to the time of arrival of impact at each sensor. Capineri et al. [21] used a sensor network of flexible piezo-polymer transducers to detect artificial defects by calculating a damage index (DI) based on the distortion and amplitude of two signals from the same path in intact and damaged conditions.

Mustapha and Ye [22] studied the characteristics of guided waves and their interaction with tapered sandwich structures with foam core.

<sup>1</sup>Corresponding author.

Manuscript received March 29, 2019; final manuscript received June 27, 2019; published online July 16, 2019. Assoc. Editor: Wieslaw Ostachowicz.

They proposed algorithms for the detection and localization of multiple defects using an active sensor network. Further, Mustapha et al. [23] and Fakhri et al. [24] investigated the use of ultrasonic guided waves to detect BVID in CF/EP sandwich composites. They presented three algorithms based on the time-reversal method, a wave-attenuation-based method, and symbolic dynamics (SD). Recent work by Sikdar et al. [25] investigated the interaction of BVID resulting from low-velocity impact damage with various Lamb-wave modes. The authors found that exciting  $A_0$  mode at 100 kHz is highly sensitive to BVID. Moreover, the authors applied the frequency-wavenumber method for damage visualization.

While detection of BVID using Lamb waves has been proved possible, localization accuracy depended on many factors such as the damage size, the used excitation frequency, the captured/investigated wave mode, and the employed DI or data processing technique [22–24]. This raises the importance of finding a robust method that can improve the localization resolution. Further, many researchers have been tackling the problem of assessment/classification of different kinds of damage [26–29]. However, due to their very small sizes, assessment or severity classification of BVIDs requires even higher sensitivities of the employed frequencies, modes, and DIs/data processing techniques. Thus, merging information from multiple frequencies, modes, and DIs/algorithms may help in reducing the uncertainties in both damage localization and prediction/classification.

This study focused on the development of an algorithm that fuses the damage signatures from various approaches (damage detection algorithms) to enhance the detection, localization, and classification of BVID in composite sandwich structures using guided waves. Damage indices based on amplitude variation (AV), SD, and root-mean-square deviation (RMSD) were merged together to give a total anomaly (TA) damage index. In addition, the algorithm combines the data collected using multiple excitation frequencies together with multiple damage signatures. An imaging algorithm was adopted to localize the damage based on the TA vector obtained from each path. Furthermore, a distance-based classification technique was proposed to classify the various damage states.

## 2 Experimental Setup

Composite sandwich panels were manufactured using CF/EP woven fabric prepreg, consisting of surface CF/EP laminates in a quasi-isotropic configuration [ $\pm 45, 0/90$ ]s with a nominal thickness of 0.88 mm, and a Nomex honeycomb core (HRH-10-1/8-3) of 20.4 mm in thickness. The CF/EP laminate was initially cured in an autoclave following the required procedures. The surface CF/EP laminates and the core were bonded together with FM 1515-3 film adhesive using secondary bonding in the autoclave [23]. Sandwich panels were trimmed to dimensions of 560 mm by 560 mm (shown in Fig. 1(a)). The properties of the sandwich panels are summarized in Table 1. The specimens were simply supported during the experiment.

A sensor network consisting of 16 circular PZTs was surface mounted on a plate. The PZT elements were distributed to enclose a square area as shown in Fig. 1(b), where the distance between neighboring PZT elements is 100 mm. Each PZT element is a circular wafer of 10 mm diameter and 1 mm thickness. During testing, one PZT element functioned as the actuator while the others functioned as sensors, and the role of the actuator alternated until all the PZT elements had functioned as the actuator. Seven cycles sinusoidal tone bursts (90 V peak-to-peak) enclosed in a Hann window were used as the input signal for the actuator. Activation and acquisition of wave signals were performed using an active signal generation and data acquisition system developed on the VXI platform, consisting mainly of a signal generator (Agilent<sup>®</sup> E1441), signal amplifier (PiezoSys<sup>®</sup> EPA-104), signal conditioner (Agilent<sup>®</sup> E3242A), and signal digitizer (Agilent<sup>®</sup> E1437A). The wave signals were captured at a sampling rate of 20.48 MHz.

The quasistatic indentation process was conducted on the sandwich composite panel using a steel indenter with a semispherical headset (Fig. 1(a)). BVID was produced, on the same panel, after 2, 3, and 5 mm indentations. The position of the indentation was maintained for the three cases. After the indenter was removed, the skin was partially pushed back up, but a dent in the skin remained due to the damage that had occurred in the core (crushing) and the skin (e.g., fiber breakage, matrix cracking, and delamination).

After each indentation, the deformation on the plate surface, defined as the residual deformation, was measured using a dial indicator gauge. It was observed that the residual deformation depth increased with the increase in the indentation depth. The 2, 3, and 5 mm indentations resulted in peak residual deformations of 0.2, 0.5, and 2.7 mm, respectively.

Four excitation frequencies (150, 175, 200, and 250 kHz) were used to excite the Lamb waves, and the data were collected from the sensor network for the healthy panel and each of the three damage cases. Eighty distinct sensing paths were available from the network (ignoring paths on the boundaries of the network such as sensing paths 1 and 2). Each recorded signal had a length of 5000 data points.

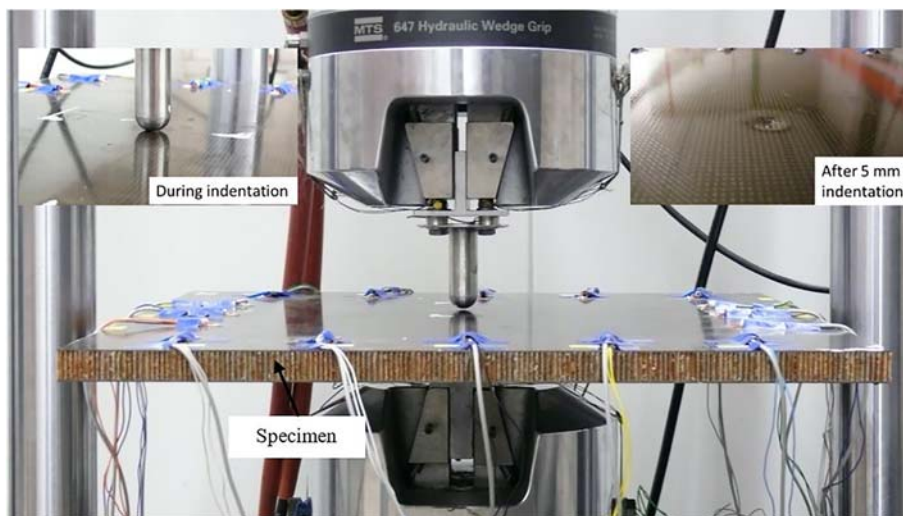
## 3 Proposed Methodology

**3.1 Data Preprocessing.** After data acquisition, preprocessing was performed for all the measured signals. The fundamental symmetric  $S_0$  mode was highly sensitive to debonding, as its magnitude decreased significantly after interacting with the debonding [23]; therefore, it was selected to interrogate the structure under study. Figure 2 shows a typically captured signal and a zoomed-in portion of the response showing the  $S_0$  mode used for this investigation. The  $S_0$  mode was identified based on previous dispersion analysis performed by Mustapha et al. [23], Mustapha and Yi [30], and Mustapha et al. [31] on the same composite sandwich structure.

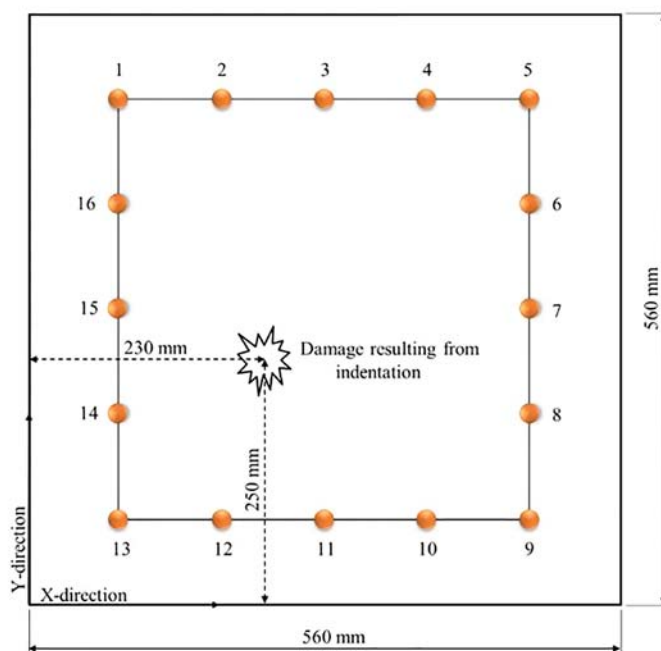
As a first step, the vertical shift in the amplitude of the signals (vertically in Fig. 2) was adjusted to zero. The  $S_0$  mode was then identified as the first transmitted wave packet since it is known to be the fastest mode existing at the excited frequencies. A starting point was chosen in each signal based on the expected position of the  $S_0$  mode according to its known group velocity [30,31]. At the used excitation frequencies, the group velocity of the  $S_0$  mode ranged between 3200 and 3700 m/s [30,31]. After that, the  $S_0$  mode was separated by keeping only the data points falling between the first seven wave peaks located after the chosen starting point. This was followed by eliminating the outliers induced due to operational conditions. Outliers were identified as signals showing significant attenuation in their response while their sensing path is far from the known position of the damage. This required the comparison of the response amplitudes between signals measured after the 5-mm indentation and the benchmark signals. The cutting and cleaning process was semiautomated, i.e., it included some manual interference, to make sure it was performed accurately and without any errors that may affect the results.

Working in the time domain, data normalization might adversely affect the quality of the signals and mask the presence of damage-sensitive features extracted; therefore, no data normalization was applied on the signals.

Figure 3 shows plots of typical preprocessed measurements of a damaged sensing paths (7–14), taken at 250 kHz excitation frequency, for the healthy state compared with the three studied damaged states (0.2-mm, 0.5-mm, and 2.7-mm dents). The path was chosen since it passes through the damage (Fig. 1) in order to visualize the damage influence on the signals. This influence will be later quantified using the different employed DIs. As was mentioned earlier, the used portion of the signals was the data points falling between the first seven wave peaks located after the chosen starting point.



(a)



(b)

**Fig. 1** CF/EP sandwich composite panel: (a) quasistatic loading and the resulting dent and (b) PZT sensor network mounted on the surface of the panel

**Table 1** Properties of CF/EP sandwich panel

Properties of plain-woven fabric CE/EP composite laminate								
$E_{11}$	$E_{22}$	$G_{12}$	$G_{23}$	$G_{31}$	$\nu_{12}$	$\nu_{13}$	$\nu_{23}$	Density
55.8 GPa	55.8 GPa	3.65 GPa	3.65 GPa	3.65 GPa	0.06	0.05	0.38	1600 kg/m <sup>3</sup>
Properties of Nomex core (HRH 10 1/8-3)								
Cell diameter				Core thickness				Density
3.2 mm				20.4 mm				48 kg/m <sup>3</sup>
Properties of Nomex material								
$E$				$\nu$				Density
3.6 GPa				0.3				1380 kg/m <sup>3</sup>

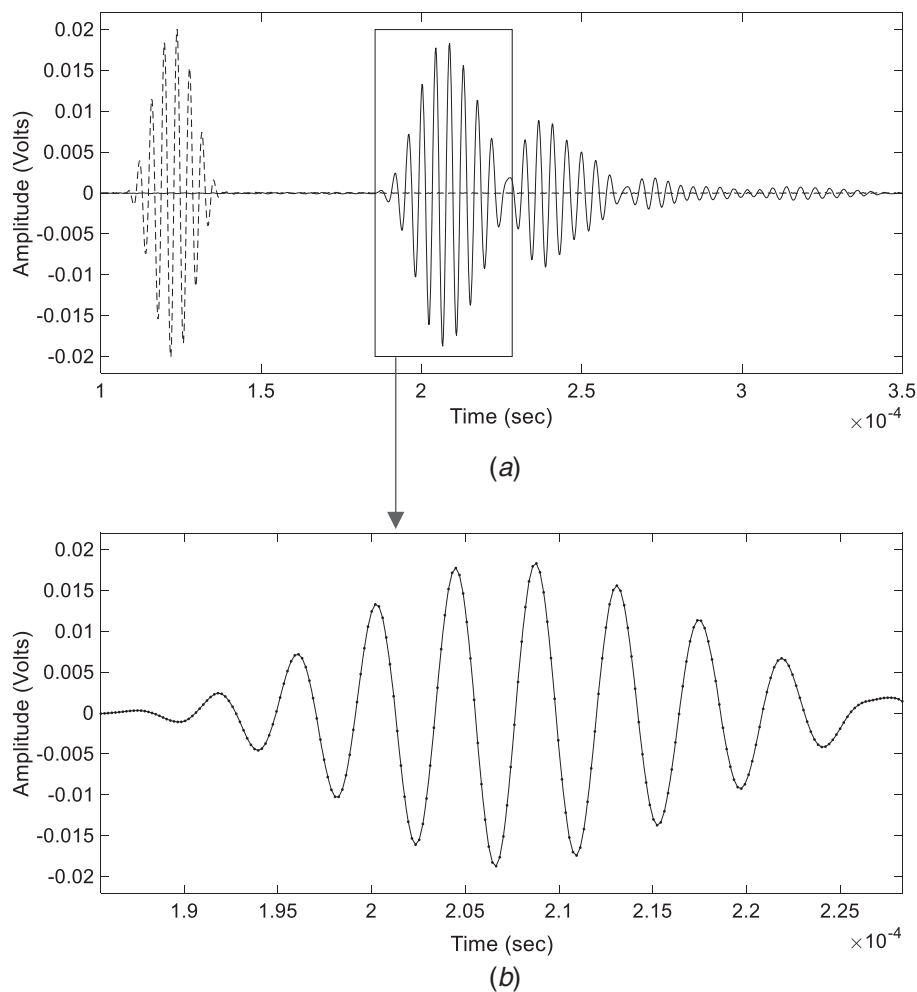


**Fig. 2 (a) Input signal for wave excitation (dashed) and the captured response (solid) and (b) the extracted  $S_0$  mode**

**3.2 Employed Anomaly Measures.** The lack of data from real damaged structures, and the infeasibility of simulating all types and severities of damage in laboratories, make it necessary to improve anomaly detection methods that can detect variations in the monitored structures based on the available data from the healthy or the current state of the structure.

Recently, RMSD [32] and SD [33–35] have been introduced to characterize time series responses in many applications including SHM. RMSD is a time domain DI which combines both RMS-based DI and variation-based DI [36]. It showed great potential in Lamb-wave anomaly detection with its ability to consider both amplitude variation and time shift in the signals [32]. On the other hand, minimum work has been done on the application of SD to ultrasonic waves; besides the work by Gupta et al. [37], where a D-Markov machine was constructed and used for the early detection and online monitoring of fatigue damage in polycrystalline alloys (7075-T6 aluminum) subjected to low-cycle and high-cycle fatigue. However, damage assessment using SD is becoming more recognized due to many successful applications. In 2009, Rao et al. [38] published a comparative review to evaluate the efficiency of SD in detecting early damage compared with other methods such as the principal component analysis, artificial neural networks, and kernel regression analysis. SD showed a good performance in terms of early detection and computational efficiency. The study was based on time series collected from a nonlinear active electronic system.

Authors of the current work [24] have demonstrated the ability of SD in the detection and localization of BVID in CF/EP sandwich structures. The smallest BVID (0.2-mm dent) was successfully

detected but not precisely localized. SD has been demonstrated to enhance the signal-to-noise ratio and perform data reduction. The used SD-based DI was shown to have an indication of the damage severity. For the same data set, Mustapha et al. [23] have previously presented two damage detection algorithms based on wave-attenuation and time-reversal techniques. Both techniques were capable of detecting the small variation of the surface condition of the panel, but the attenuation-based approach performed better in terms of damage localization.

To increase the robustness of damage localization and assessment, the methodology proposed in this work is to fuse results from different excitation frequencies and damage-sensitive features, namely, AV, SD, and RMSD. The healthy response of each sensing path was considered as the benchmark of this specific path, and the three anomaly measures were calculated then merged together as will be elaborated in Secs. 3.3 and 3.4.

The first anomaly measure, AV, is a direct comparison between the amplitude of the  $S_0$  mode before and after indentation. The amplitude of the middle peak, third peak in this case and usually the highest peak, of the  $S_0$  mode was considered. The AV DI was defined as in Eq. (1):

$$AV = \left| 1 - \frac{\text{amplitude}(\text{third peak}(S_d))}{\text{amplitude}(\text{third peak}(S_b))} \right| \quad (1)$$

where  $S_b$  and  $S_d$  are the  $S_0$  mode extracted from the signals measured before (benchmark) and after introducing the damage, respectively.

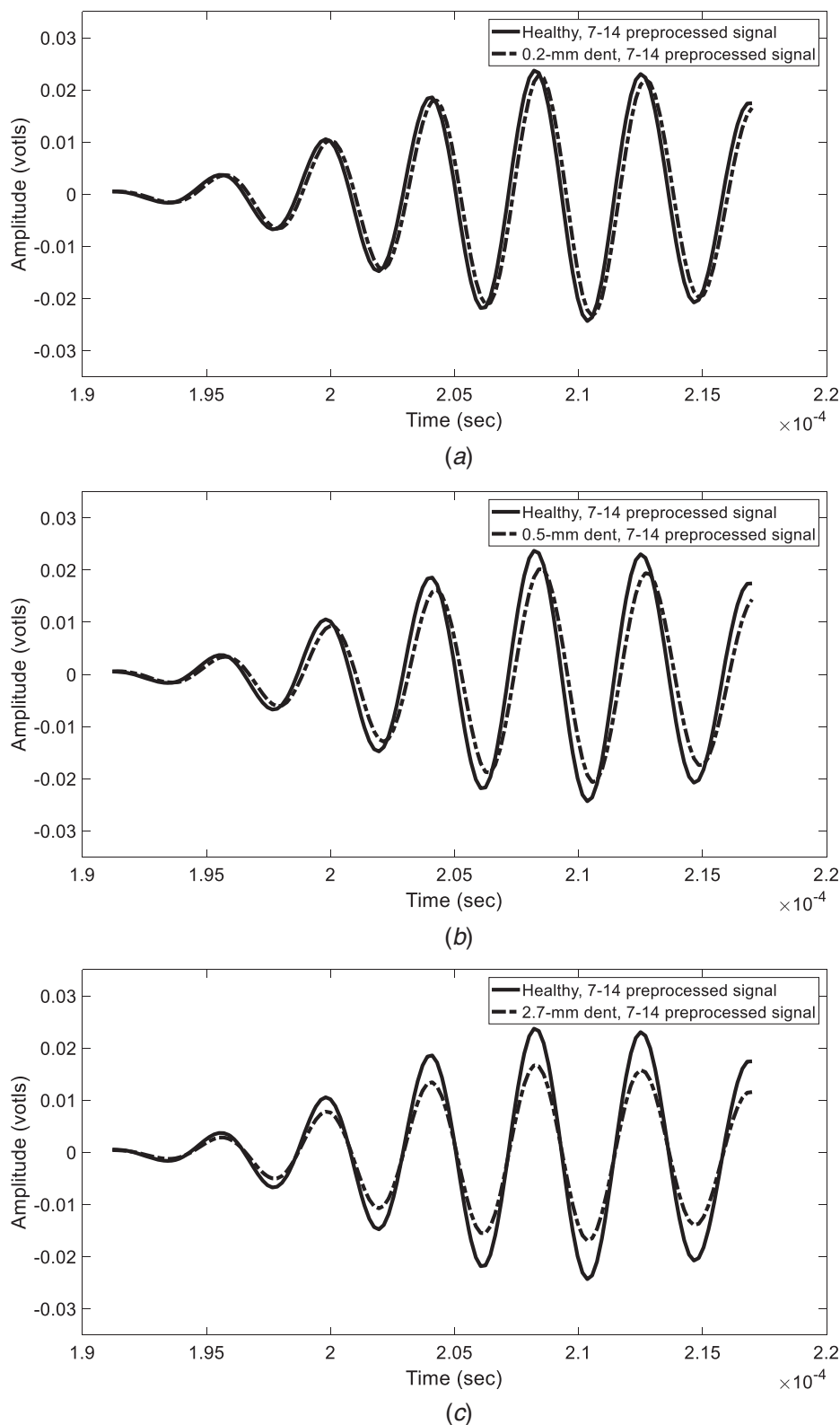


**Fig. 3 Typical preprocessed measurements of a damaged sensing paths (7-14), taken at 250 kHz excitation frequency, for the healthy state compared with damaged states of the (a) 0.2-mm dent, (b) 0.5-mm dent, and (c) 2.7-mm dent**

The second damage signature, SD, was based on the symbolic time series analysis (STSA) introduced in the author's previous work [24]. STSA transforms the time series data into symbol sequences according to a preconstructed symbol space using a set number of partitions. A distinct symbol space is built for every single path based on the

benchmark measurement in the healthy state. The number of partitions selected was determined based on the maximization of Shannon's entropy to avoid the loss of important information. Twenty partitions were used in this study as this number of partitions gave the highest accuracy in the previous investigation.

After partitioning the signal into ranges of symbols, the signal will be represented by a probability vector indicating the probability of occurrence of each symbol in the signal (symbol sequence), thus reducing the data size from the original data points into 20 data points. This data reduction significantly reduces computational time. The SD anomaly measure was calculated based on Eq. (2):

$$SD = \left| 1 - \frac{\|V_d\|}{\|V_b\|} \right| \quad (2)$$

where  $\|V_b\|$  and  $\|V_d\|$  are the norms of the probability vectors in the intact (nominal) and the damaged states, respectively.

The third anomaly measure, RMSD, is a measure that incorporates both the amplitude change and the time shift between two signals. RMSD is calculated by measuring the amplitude deviation of all the data points in comparison with their corresponding data points in the benchmark signal, according to Eq. (3):

$$RMSD = \sqrt{\frac{\sum_{i=0}^{N-1} (S_d(i) - S_b(i))^2}{\sum_{i=0}^{N-1} S_b(i)^2}} \quad (3)$$

where the index  $i$  corresponds to the  $i$ th data point of the signal.

The three calculated DIs would give different anomaly measures for the same sensing path. Thus, a proper normalization should be applied before merging different DIs together. The proposed normalization method was to calculate the ratio of the anomaly values of all the sensing paths with respect to the path with the highest DI. Each of the three distinct DIs was normalized among all the sensing paths to give a range between [0,1] from the least damaged path to the most damaged path. In this way, the normalized DIs will all have comparable values resembling the ranking of the considered path's damage as compared with the path of the highest damage.

**3.3 Frequency Fusion of Single Damage Indices.** After normalizing the three extracted DIs, each single DI was first treated separately. Since data is available from four excitation frequencies (150, 175, 200, and 250 kHz), each path will have four values of any specific DI (e.g., AV) corresponding to the excitation frequencies. To minimize the effect of changing the frequency on the damage prediction, the anomaly of each path was considered as the average of the four values (computed from different frequencies), which was defined as

$$DI_{\text{combined frequency}} = \text{mean}(DI_{150 \text{ kHz}}, DI_{175 \text{ kHz}}, DI_{200 \text{ kHz}}, DI_{250 \text{ kHz}}) \quad (4)$$

where  $DI$  may be AV, SD, or RMSD.

**3.4 Frequency and Damage Indices Fusion: Total Anomaly.** The three extracted DIs (AV, SD, and RMSD) from the

four excitation frequencies were fused together in a one anomaly measure which was given the name of TA. This was performed by averaging all the available values of DIs (from the considered frequencies), for each path, to give one TA, according to Eq. (5):

$$TA = \text{mean}(AV_{\text{considered frequency}(ies)}, SD_{\text{considered frequency}(ies)}, RMSD_{\text{considered frequency}(ies)}) \quad (5)$$

The flowchart summarizing the methodology for damage detection, localization, and assessment proposed in this paper is shown in Fig. 4. Damage localization and assessment, based on the obtained anomaly measures, will be discussed in Secs. 3.5 and 3.6.

**3.5 Data Fusion and Damage Localization.** From the network of 16 PZT elements in the panel, 240 sensing paths are available. Due to the dual function of the PZT elements, the number of paths can be reduced to 120 distinct paths (e.g., instead of using both paths 1-6 and 6-1, only 1-6 is considered). After neglecting the paths connecting sensors on the same edges (e.g., paths 1-2, 1-4, and 14-16), the paths are further reduced to 80 relevant paths which are shown in Fig. 5. The TA measures obtained for these 80 paths were employed to construct a damage image (using data fusion technique). The damage is expected to be located on the intersection of the most damaged paths, i.e., the paths having the highest anomaly measures.

Construction of the damage image was accomplished by dividing the monitored zone into uniform  $1 \text{ mm}^2$  square-shaped grid points, where the existence of damage in each cell is evaluated by merging the perceptions of the anomaly measures from all the sensing paths in that cell.

The DI or the probability of damage at a cell  $(x, y)$  in the observed zone is given by [39]

$$DI(x, y) = \sum_{j=1}^J P_j(x, y) = \sum_{j=1}^J TA_j f_j(z) \quad (6)$$

where  $P_j(x, y)$  is the probability of damage at cell  $(x, y)$  obtained from the anomaly measure of the  $j$ th path,  $TA_j$  is the TA measure for the  $j$ th path, and  $f_j(z)$  is the normal distribution function for the  $j$ th path (defined below).

To account for the possible existence of damage near the paths, the influence of the anomaly measure is considered in the shape of a normal distribution function having a maximum effect on the path and decreasing away from it. This normal distribution function is defined by

$$f(z) = \frac{1}{\sigma\sqrt{2\pi}} e^{-\frac{(z-\mu)^2}{2\sigma^2}} \quad \text{for } -\infty < z < +\infty \quad (7)$$

where  $\mu$  is the mean of the normal distribution model and  $\sigma$  is the standard deviation of the normal distribution model.

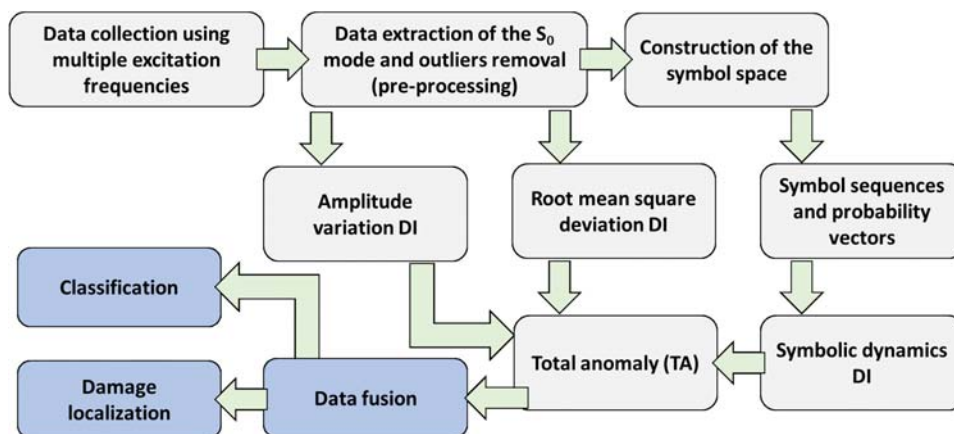


Fig. 4 A flowchart for the damage detection, localization, and assessment algorithm

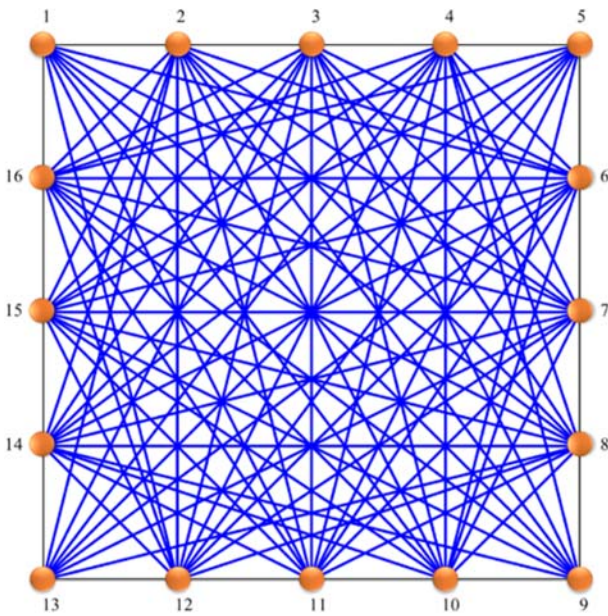


Fig. 5 The sensing paths used in the data fusion (80 paths)

Since the effect of damage at a point located along the sensing path is stronger than a damage located at a distance from the sensing path,  $\mu$  was set to be equal to zero.

On the other hand, an experimental investigation was performed to determine the proper value of  $\sigma$  for the used sandwich structure [23]. The study has found that the effect of a damage located at a point further than 40 mm from the sensing path is negligible. For this reason,  $\sigma$  was fixed at 40 mm.

Further,  $z$  was determined by assigning the same effect of damage for all the grid points that were equidistant from the path. This was conducted by considering a rectangular affected zone for each sensing path during the fusion process where  $z$  was defined as the normal distance separating the grid point from the  $j$ th sensing path. During the fusing process, the rectangular region assigns the same sensation of the damage for grid points that are equidistant from the sensing path (or that have the same value of  $z$ ) [40].

**3.6 Damage Classification.** A distance-based classification technique was proposed in this work. Three clusters (0.2, 0.5, and 2.7-mm dent sizes) were generated from the labeled training tuples. Based on the built clusters, the new data (or the testing tuple) is classified considering its distance from the mean of each

cluster. To have an indication of the damage severity, the considered classification feature was the average anomaly measure of all the available sensing paths (excluding the removed outlier paths). Different trials were made considering single DIs, multiple DIs, and TA (using single frequencies). For more clarity, the algorithm will be explained for the case of taking TA as the anomaly measure. The algorithm works as follows:

- (1) Twelve tuples (samples, records, or instances) are available for classification (three dent sizes  $\times$  four frequencies).
- (2)  $TA_{\text{average}}$  is calculated as the mean of the TA of all the sensing paths, for each of the 12 tuples.  $TA_{\text{average}}$  is the only feature that will be used to classify each tuple as 0.2, 0.5, or 2.7-mm dent size.
- (3) Leave-one-out cross-validation (LOOCV) was used to test the model on every single tuple (of the 12 tuples), and then the total accuracy of all the 12 tests was calculated. LOOCV is applied as follows (refer to Fig. 6):
  - (a) One tuple is chosen for testing, and the remaining 11 tuples are used for training.
  - (b) Training consists of determining the three means of the three clusters/classes (corresponding to the three damage cases). A mean of a cluster is simply the average feature of the tuples belonging to it ( $TA_{\text{average}}$  is the only feature in this case), e.g., if the training data contains four tuples labeled as 2.7-mm dent size, the mean of the 2.7 dent cluster is the mean of the  $TA_{\text{average}}$  of those four tuples.
  - (c) The distances between the testing tuple and the three means (determined in (b)) are calculated.
  - (d) The testing tuple is given the label of the nearest mean, e.g., in Fig. 6, the distance between the testing tuple and the mean of "Cluster 2" is smaller than those from the other two means, hence, this testing tuple will be classified as belonging to "Cluster 2".
  - (e) If the classification was correct (based on the known true label of the testing tuple), it is given an accuracy of 100%, otherwise, an accuracy of 0% is given to the classification (since there is only one testing tuple).
  - (f) The process from (a) to (e) is repeated 12 times so that every single tuple serves as a testing tuple.
- (4) The final classification accuracy is the average of all the accuracies calculated in step (3) (12 accuracies having the values of 0% or 100%).

Due to the small amount of available data (only 12 tuples each of a single feature), testing the accuracy of the algorithm on each single tuple is important to prove its validity. Figure 6 presents an illustration clarifying the used classification process.

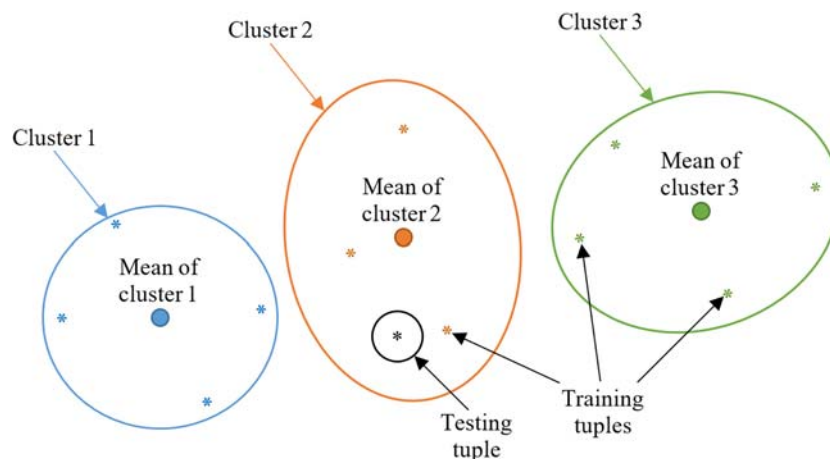
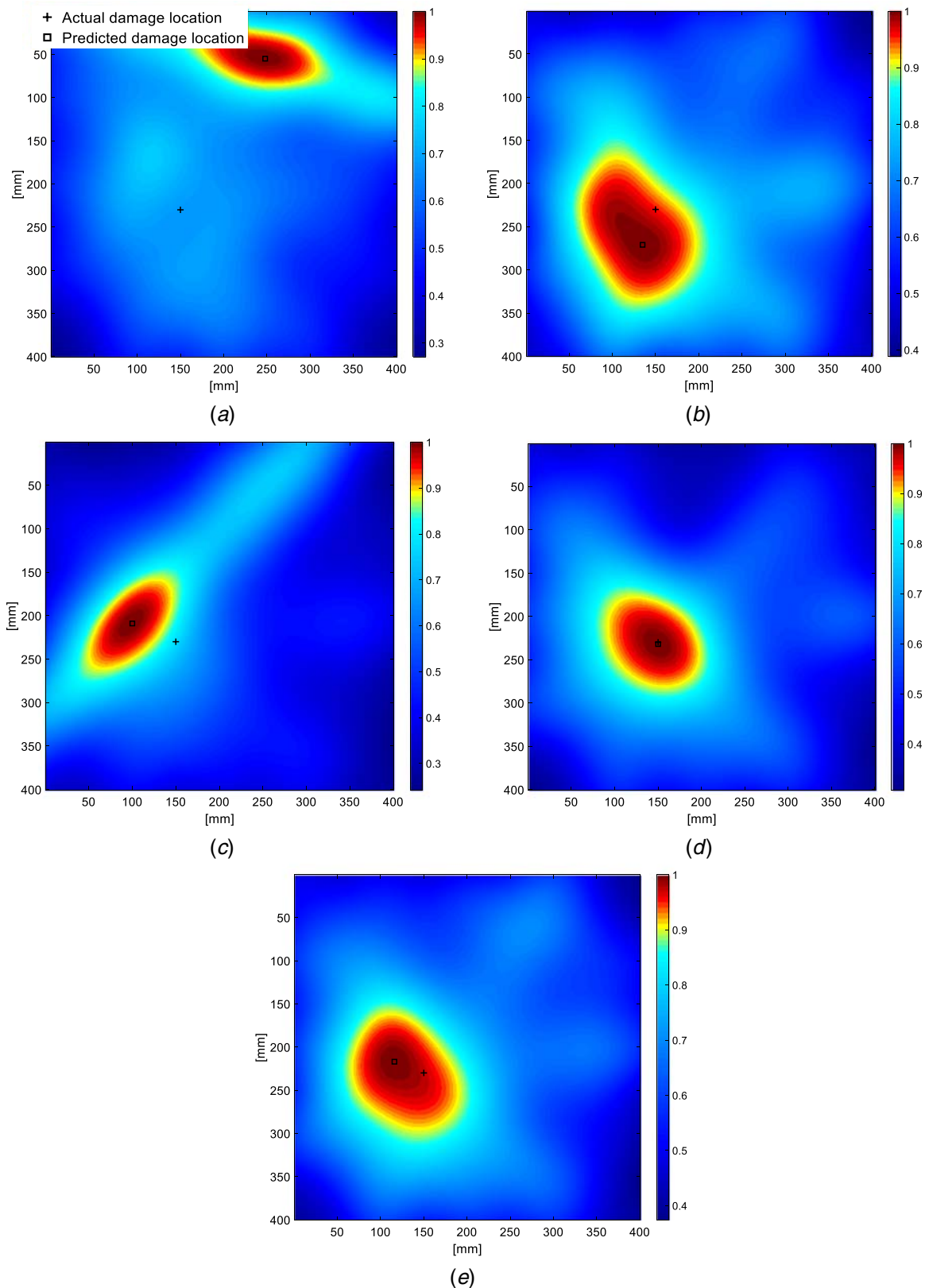


Fig. 6 An illustration of the used classification algorithm

## 4 Results and Discussion

**4.1 Damage Localization—Frequency Fusion.** Data were fused combining the four excitation frequencies and using the defined damage indices described earlier. An example of the

image reconstruction is shown in Fig. 7 using the AV damage index after indenting displacement of 3 mm (resulting in a dent of 0.5 mm). Figure 7 compares the results for individual frequencies (Figs. 7(a)–7(d)) and frequencies combined (Fig. 7(e)). The error between the actual and predicted damage locations was calculated



**Fig. 7** Image reconstruction using various excitation frequencies after 3-mm indentation (0.5-mm dent): (a) 150 kHz, (b) 175 kHz, (c) 200 kHz, (d) 250 kHz, and (e) combined frequency reconstruction

**Table 2 Prediction of damage location by combining the results of various frequencies using a single damage index**

Dent size (mm)	Distance between predicted and actual damage locations (mm)				
AV					
0.2	239.9	122.7	133.4	44.0	48.1
0.5	200.6	43.7	54.2	2.0	36.4
2.7	19.2	10.0	13.0	12.4	8.5
Frequency (kHz)	150	175	200	250	Combined frequencies
SD					
0.2	233.0	122.3	88.8	132.4	93.3
0.5	200.8	41.3	53.3	46.8	37.6
2.7	23.0	13.0	18.0	17.1	13.0
Frequency (kHz)	150	175	200	250	Combined frequencies
RMSD					
0.2	92.3	138.1	79.3	39.7	61.4
0.5	195.9	29.2	78.0	123.6	68.0
2.7	15.8	5.7	5.1	19.0	10.4
Frequency (kHz)	150	175	200	250	Combined frequencies

**Table 3 Prediction of damage location using the results of combining all damage indices from various frequencies**

Dent size (mm)	Distance between predicted and actual damage locations (mm)						
0.2	227.3	115.7	79.9	42.6	69.9	78.9	78.0
0.5	193.3	28.1	62.8	93.0	53.2	44.9	45.9
2.7	15.0	9.2	11.0	16.0	14.0	12.2	10.8
Frequency (kHz)	150	175	200	250	200 and 250	175, 200, and 250	All frequencies

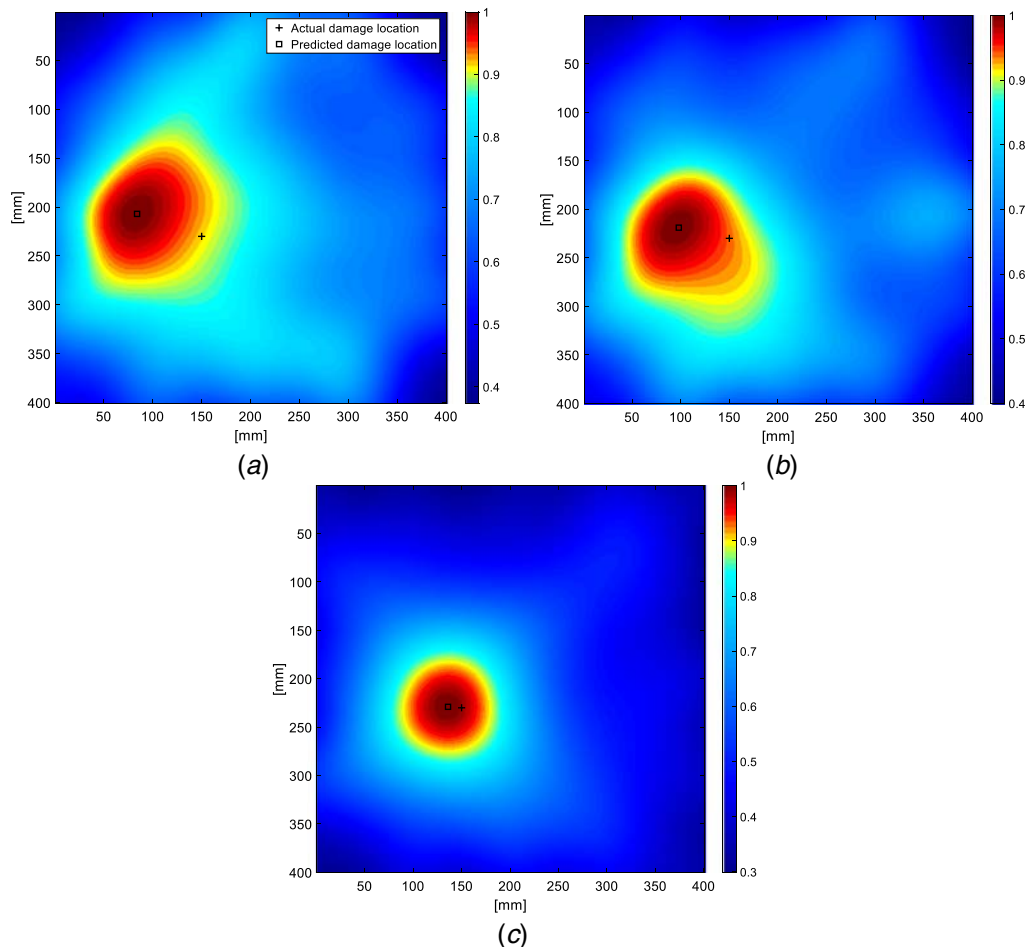


**Fig. 8 Image reconstruction using combined damaged indices of 200 and 250 kHz: (a) 0.2-mm dent, (b) 0.5-mm dent, and (c) 2.7-mm dent**

as the Euclidean distance ( $L^2$  norm) between the two positions using their  $x$ - $y$  coordinates.

Using an excitation frequency of 150 kHz, the error between the actual and predicted location of damage is 200 mm, while exciting at 250 kHz, the results improve dramatically, leading to an error of 2 mm (shown in Table 2). Similar observations were made for the 0.2 and 2.7-mm dents. It is very clear that the precision in damage localization is highly dependent on the excitation frequency. In Fig. 7(e), using the frequencies combined, the result shows good consistency in localizing the BVID, however, with a slight reduction in the accuracy, in some cases (Table 2). Combining frequencies has resulted in the same accuracy as the best frequency did for the 2.7-mm dent based on SD or even in a better accuracy in the case of 2.7-mm dent using AV, and 0.5-mm dent using SD.

As obviously seen from Table 2, the damage was reliably identified in all the three tested cases, even in the case of the smallest surface dent of 0.2 mm resulting from 2-mm indentation. Furthermore, the damage localization based on SD and RMSD led to the same conclusion that the 150 kHz and 175 kHz lack the ability to localize the damage precisely (mainly for the small dents of 0.2 and 0.5 mm), as shown in Table 2. Again, the approach of combining the damage indices from the four frequencies showed a major improvement and robustness in damage localization.

#### 4.2 Damage Localization—Frequency and Damage Indices

**Fusion.** The results of combining the three damage indices (AV, SD, and RMSD) using two and three excitation frequencies are compared with those when combining all the excitation frequencies.

The results show some discrepancy as observed in Table 3. Using an excitation of 150 kHz to identify the dent of 0.2 mm resulted in 227.3-mm distance between the actual and predicted locations. This error varies randomly and is not a function of frequency, for instance with the 0.5-mm dent, the error was reduced dramatically when changing the excitation frequency from 150 kHz to 175 kHz, and then increased significantly when exciting at 250 kHz.

Joining the data from two excitation frequencies (200 + 250 kHz) showed a clear consistency and improvement in the results for all the damage cases and in particular for the 0.2-mm dent. The resulting reconstructed images are shown in Fig. 8, for the three dent sizes. Although the prediction accuracy dropped slightly when compared with some results corresponding to a single frequency, however combining the data from multiple frequencies shows consistency in the prediction (as shown in Table 3). Including the data of all the excitation frequencies showed a further improvement and consistency in the localization for the 0.2 and 2.7-mm dent. The resulting reconstructed images for the combined frequencies are shown in Fig. 9.

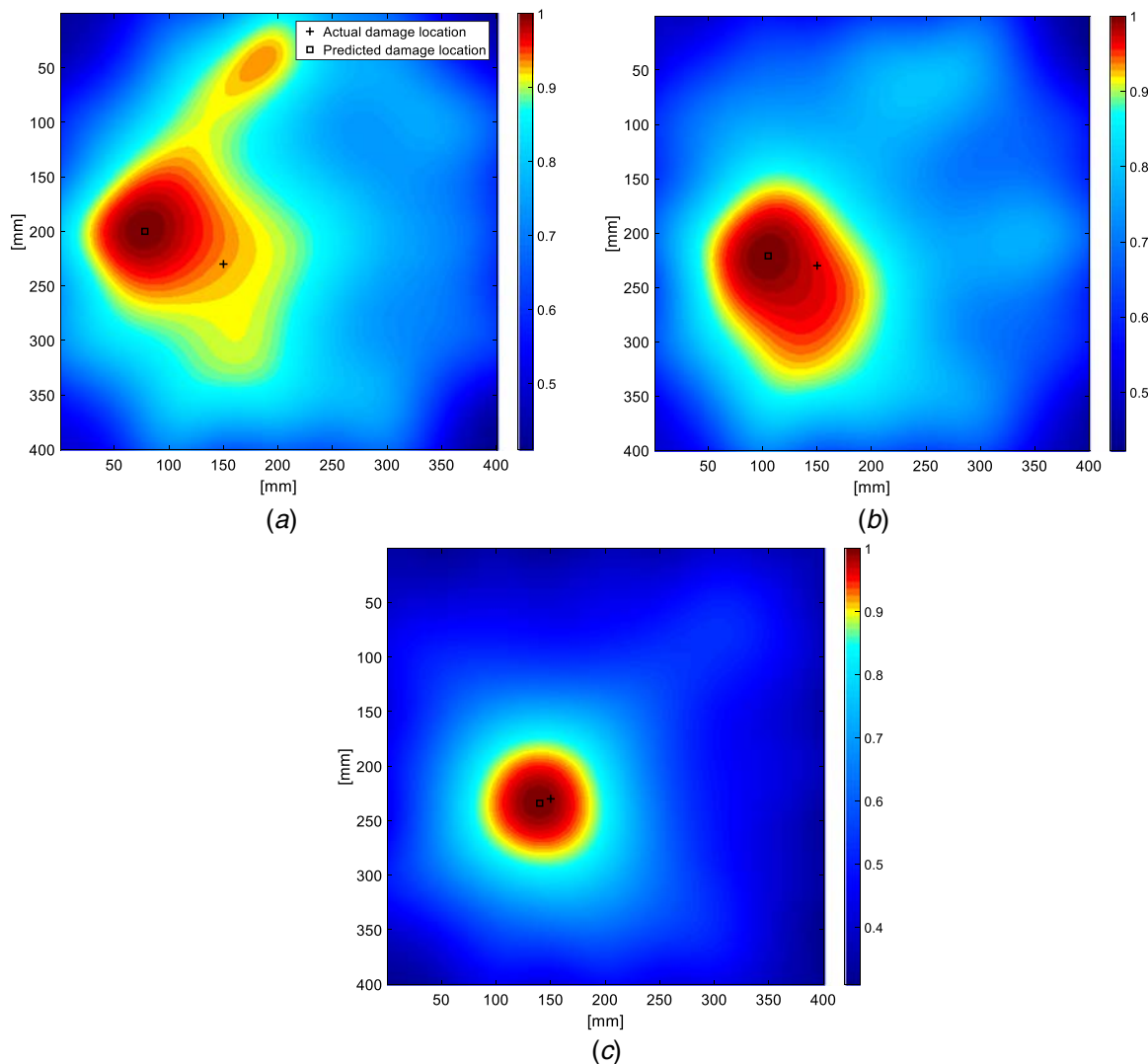


Fig. 9 Image reconstruction using combined damaged indices of the four frequencies: (a) 0.2-mm dent, (b) 0.5-mm dent, and (c) 2.7-mm dent

**Table 4 Classification of indentation**

Dent size (mm)	Original tuples				Classification accuracy (%)	Normalized tuples				Classification accuracy (%)
Average total anomaly ( $TA_{\text{average}}$ )										
0.2	0.05	0.06	0.07	0.07	91.67	0.46	0.50	0.57	0.52	91.67
0.5	0.07	0.08	0.10	0.10		0.61	0.64	0.82	0.71	
2.7	0.12	0.12	0.12	0.14		1.00	1.00	1.00	1.00	
Frequency (kHz)	150	175	200	250		150	175	200	250	
Average amplitude variation ( $AV_{\text{average}}$ )										
0.2	0.02	0.02	0.02	0.01	100	0.22	0.17	0.18	0.13	100
0.5	0.04	0.05	0.06	0.04		0.48	0.58	0.69	0.54	
2.7	0.09	0.09	0.09	0.08		1.00	1.00	1.00	1.00	
Frequency (kHz)	150	175	200	250		150	175	200	250	
Average symbolic dynamics ( $SD_{\text{average}}$ )										
0.2	0.03	0.03	0.04	0.05	58.33	0.43	0.46	0.46	0.54	100
0.5	0.04	0.04	0.06	0.06		0.61	0.61	0.78	0.69	
2.7	0.06	0.07	0.08	0.09		1.00	1.00	1.00	1.00	
Frequency (kHz)	150	175	200	250		150	175	200	250	
Average root-mean-square deviation ( $RMSD_{\text{average}}$ )										
0.2	0.12	0.14	0.16	0.15	58.33	0.58	0.65	0.76	0.64	66.67
0.5	0.14	0.15	0.19	0.18		0.67	0.68	0.89	0.77	
2.7	0.20	0.21	0.21	0.24		1.00	1.00	1.00	1.00	
Frequency (kHz)	150	175	200	250		150	175	200	250	

**4.3 Damage Classification.** All accuracy values mentioned in this section are the average accuracy of a LOOCV of the used classifier. LOOCV was used to make sure that the classifier is performing well for every single tuple. This was mainly because of the small available number of tuples (three damage cases  $\times$  four excitation frequencies = 12 tuples). Table 4 shows the results of classification using single DIs and TA as features. For each feature, classification was done before and after normalizing the tuples of the same frequency but of different damage sizes (columns in Table 4). Normalization was done to ensure a similar comparison between values coming from different excitation frequencies which has shown a dramatic accuracy improvement in the case of SD.

The accuracy of the distance-based classification approach was 91.67% when using the  $TA_{\text{average}}$  as a feature. A 100% accuracy was obtained for the individual damage indices based on both the AV and SD. On the other hand, when repeating the analysis using the RMSD the accuracy did not exceed 70%. Further, putting all the normalized tuples of Table 4 together ( $12 \times 4 = 48$  tuples) and applying the same classification procedure resulted in an accuracy of 83.33%. The high classification accuracies attained shows the high correlation between the extracted DIs and the size of BVID.

### 5 Concluding Remarks

In this study, different anomaly detection approaches were compared together in terms of the detection, localization, and assessment of barely visible indentation damages in sandwich composite structures, and a new fusion approach was proposed. Ultrasonic measurements from a surface-mounted sensor network were collected for healthy and three progressive damage conditions. Data fusion techniques were proposed to increase the robustness of damage localization by merging measurements from various excitation frequencies and using three different damage indices, based on amplitude variation, symbolic dynamics, and root mean square deviation.

Combining results from different excitation frequencies for a single DI was proved to increase the localization consistency while keeping high accuracy level. Even the smallest damage size (0.2-mm dent) was successfully detected and was localized with a good accuracy. Furthermore, TA measure was suggested to be the damage index combining the effects of all the three single DIs and the four excitation frequencies. TA showed high

robustness in BVID detection and localization for the three tested dent sizes.

A distance-based classification technique was proposed and tested on the single DIs, multiple DIs, and on the TA. Anomalies of all the available sensing paths were averaged to give one value used as a single classification feature. Classification accuracies of above 90% were attained for all the used DIs except for RMSD which gave an accuracy of less than 70%.

Lamb waves, along with the proposed methodology, demonstrated high sensitivity to detect small changes on the surface of the structure under study, in addition to their ability in localizing and assessing the detected damage.

### Acknowledgment

Recognition and gratitude are addressed to the Lebanese National Council for Scientific Research (CNRS) (Funder ID: 10.13039/501100005993) for their Awards No. 103085 and their Ph.D. scholarship provided to the first author. The financial support of the University Research Board at the American University of Beirut (Funder ID: 10.13039/100007688) for their Award No. 103187 is also acknowledged.

### References

- [1] Yu, L., Tian, Z., Li, X., Zhu, R., and Huang, G., 2019, "Core-Skin Debonding Detection in Honeycomb Sandwich Structures Through Guided Wave Wavefield Analysis," *J. Intell. Mater. Syst. Struct.*, **30**(9), pp. 1306–1317.
- [2] Sikdar, S., and Banerjee, S., 2017, *Structural Health Monitoring of Advanced Composites Using Guided Waves: Online Monitoring of Defects/Discontinuities in Advanced Composite Structures Using Ultrasonic Guided Waves and PZTs*, LAMBERT Academic Publishing.
- [3] Kreculj, D., and Rašuo, B., 2013, "Review of Impact Damages Modelling in Laminated Composite Aircraft Structures," *Tehnički vjesnik*, **20**(3), pp. 485–495.
- [4] Minakuchi, S., Okabe, Y., Mizutani, T., and Takeda, N., 2009, "Barely Visible Impact Damage Detection for Composite Sandwich Structures by Optical-Fiber-Based Distributed Strain Measurement," *Smart Mater. Struct.*, **18**(8), p. 085018.
- [5] Meo, M., Vignjevic, R., and Marengo, G., 2005, "The Response of Honeycomb Sandwich Panels Under Low-Velocity Impact Loading," *Int. J. Mech. Sci.*, **47**(9), pp. 1301–1325.
- [6] Becz, S., Hurtado, J., and Lapczyk, I., 2007, "Analysis of Barely Visible Impact Damage for Aerospace Structures," 16th International Conference on Composite Materials, Kyoto, Japan, July 8–13, pp. 8–13.
- [7] Staszewski, W., Mahzan, S., and Traynor, R., 2009, "Health Monitoring of Aerospace Composite Structures—Active and Passive Approach," *Compos. Sci. Technol.*, **69**(11), pp. 1678–1685.

- [8] Ruzek, R., Lohonka, R., and Jironc, J., 2006, "Ultrasonic C-Scan and Shearography NDI Techniques Evaluation of Impact Defects Identification," *NDT & E Int.*, **39**(2), pp. 132–142.
- [9] Takeda, S., Aoki, Y., Ishikawa, T., Takeda, N., and Kikukawa, H., 2007, "Structural Health Monitoring of Composite Wing Structure During Durability Test," *Compos. Struct.*, **79**(1), pp. 133–139.
- [10] Rathod, V. T., and Roy Mahapatra, D., 2011, "Ultrasonic Lamb Wave Based Monitoring of Corrosion Type of Damage in Plate Using a Circular Array of Piezoelectric Transducers," *NDT & E Int.*, **44**(7), pp. 628–636.
- [11] Staszewski, W., Lee, B., and Traynor, R., 2007, "Fatigue Crack Detection in Metallic Structures With Lamb Waves and 3D Laser Vibrometry," *Meas. Sci. Technol.*, **18**(3), p. 727.
- [12] Badcock, R. A., and Birt, E. A., 2000, "The Use of 0-3 Piezocomposite Embedded Lamb Wave Sensors for Detection of Damage in Advanced Fibre Composites," *Smart Mater. Struct.*, **9**(3), p. 291.
- [13] Michaels, J. E., and Michaels, T. E., 2007, "Guided Wave Signal Processing and Image Fusion for In Situ Damage Localization in Plates," *Wave Motion*, **44**(6), pp. 482–492.
- [14] Mustapha, S., and Ye, L., 2013, "Damage Identification and Assessment in Tapered Sandwich Structures Using Guided Waves," *Key Eng. Mater.*, **558**, pp. 25–38.
- [15] Sikdar, S., and Ostachowicz, W., 2019, "Ultrasonic Lamb Wave-Based Debonding Monitoring of Advanced Honeycomb Sandwich Composite Structures," *Strain*, **55**(1), p. e12302.
- [16] Sikdar, S., and Ostachowicz, W., 2019, "Nondestructive Analysis of Core-Junction and Joint-Debond Effects in Advanced Composite Structure," *Polym. Test.*, **73**, pp. 31–38.
- [17] Sikdar, S., and Banerjee, S., 2016, "Identification of Disbond and High Density Core Region in a Honeycomb Composite Sandwich Structure Using Ultrasonic Guided Waves," *Compos. Struct.*, **152**, pp. 568–578.
- [18] Polimeno, U., and Meo, M., 2009, "Detecting Barely Visible Impact Damage Detection on Aircraft Composites Structures," *Compos. Struct.*, **91**(4), pp. 398–402.
- [19] Ross, R. W., 2006, "Structural Health Monitoring and Impact Detection Using Neural Networks for Damage Characterization," Proceedings of the 47th AIAA/ASME/ASCE/AHS/ASC Structures, Structural Dynamics, and Materials Conference, New Port, RI, May 1–4, p. 2117.
- [20] Zhang, D. C., Ouyang, L., Qing, P., and Li, I., 2008, "A Novel Real-Time Health Monitoring System for Unmanned Vehicles," SPIE Defense and Security Symposium, Orlando, FL, Apr. 22, p. 696217.
- [21] Capineri, L., Bulletti, A., Calzolari, M., and Francesconi, D., 2013, "Lamb Wave Ultrasonic System for Active Mode Damage Detection in Composite Materials," *Chem. Eng. Trans.*, **33**, pp. 577–582.
- [22] Mustapha, S., and Ye, L., 2015, "Propagation Behaviour of Guided Waves in Tapered Sandwich Structures and Debonding Identification Using Time Reversal," *Wave Motion*, **57**, pp. 154–170.
- [23] Mustapha, S., Ye, L., Dong, X., and Alamdari, M. M., 2016, "Evaluation of Barely Visible Indentation Damage (BVID) in CF/EP Sandwich Composites Using Guided Wave Signals," *Mech. Syst. Signal Process.*, **76–77**, pp. 497–517.
- [24] Fakh, M. A., Mustapha, S., Makki Alamdari, M., and Ye, L., 2017, "Symbolic Dynamics Time Series Analysis for Assessment of Barely Visible Indentation Damage in Composite Sandwich Structures Based on Guided Waves," *J. Compos. Mater.*, **51**(29), pp. 4129–4143.
- [25] Sikdar, S., Kudela, P., Radziński, M., Kundu, A., and Ostachowicz, W., 2018, "Online Detection of Barely Visible Low-Speed Impact Damage in 3D-Core Sandwich Composite Structure," *Compos. Struct.*, **185**, pp. 646–655.
- [26] Nazarko, P., and Ziemiański, L., 2017, "Anomaly Detection in Composite Elements Using Lamb Waves and Soft Computing Methods," *Proc. Struct. Integr.*, **5**, pp. 131–138.
- [27] Sbarufatti, C., Manson, G., and Worden, K., 2014, "A Numerically-Enhanced Machine Learning Approach to Damage Diagnosis Using a Lamb Wave Sensing Network," *J. Sound Vib.*, **333**(19), pp. 4499–4525.
- [28] Hameed, M. S., Li, Z., Chen, J., and Qi, J., 2019, "Lamb-Wave-Based Multistage Damage Detection Method Using an Active PZT Sensor Network for Large Structures," *Sensors*, **19**(9), p. 2010.
- [29] Satpal, S. B., Guha, A., and Banerjee, S., 2016, "Damage Identification in Aluminum Beams Using Support Vector Machine: Numerical and Experimental Studies," *Struct. Control Health Monit.*, **23**(3), pp. 446–457.
- [30] Mustapha, S., and Ye, L., 2014, "Leaky and Non-Leaky Behaviours of Guided Waves in CF/EP Sandwich Structures," *Wave Motion*, **51**(6), pp. 905–918.
- [31] Mustapha, S., Ye, L., Wang, D., and Lu, Y., 2011, "Assessment of Debonding in Sandwich CF/EP Composite Beams Using A0 Lamb Wave at Low Frequency," *Compos. Struct.*, **93**(2), pp. 483–491.
- [32] Gresil, M., and Giurgiutiu, V., 2013, "Time-Domain Hybrid Global–Local Concept for Guided-Wave Propagation With Piezoelectric Wafer Active Sensor," *J. Intell. Mater. Syst. Struct.*, **24**(15), pp. 1897–1911.
- [33] Alamdari, M. M., Li, J., and Samali, B., 2014, "Damage Localisation Using Symbolic Time Series Approach" *Dynamics of Civil Structures*, Vol. 4, Springer, New York, pp. 109–115.
- [34] Makki Alamdari, M., Samali, B., and Li, J., 2015, "Damage Localization Based on Symbolic Time Series Analysis," *Struct. Control Health Monit.*, **22**(2), pp. 374–393.
- [35] Makki Alamdari, M., Samali, B., Li, J., Ye, L., and Mustapha, S., 2017, "Structural Condition Assessment Using Entropy-Based Time Series Analysis," *J. Intell. Mater. Syst. Struct.*, **28**(14), pp. 1941–1956.
- [36] Su, Z., and Ye, L., 2009, *Identification of Damage Using Lamb Waves: From Fundamentals to Applications*, Vol. 48, Springer Science & Business Media, London.
- [37] Gupta, S., Ray, A., and Keller, E., 2007, "Online Fatigue Damage Monitoring by Ultrasonic Measurements: A Symbolic Dynamics Approach," *Int. J. Fatigue*, **29**(6), pp. 1100–1114.
- [38] Rao, C., Ray, A., Sarkar, S., and Yasar, M., 2009, "Review and Comparative Evaluation of Symbolic Dynamic Filtering for Detection of Anomaly Patterns," *Signal Image Video Process.*, **3**(2), pp. 101–114.
- [39] Wang, D., Ye, L., Su, Z., Lu, Y., Li, F., and Meng, G., 2010, "Probabilistic Damage Identification Based on Correlation Analysis Using Guided Wave Signals in Aluminum Plates," *Struct. Health Monit.*, **9**(2), pp. 133–144.
- [40] Mustapha, S., Ye, L., Wang, D., and Lu, Y., 2012, "Debonding Detection in Composite Sandwich Structures Based on Guided Waves," *AIAA J.*, **50**(8), pp. 1697–1706.